mer). These are important questions, and IC is a promising tool with which we can address these issues.

REFERENCES AND NOTES

1. J. C. Maxwell, *Philos. Mag.* **20**, 21 (1860).
2. P. Langevin, *Ann. Chim. Phys.* **5**, 245 (1905).
3. G. H. Wannier, *Bell Syst. Tech. J.* **32**, 170 (1953); *Phys. Rev.* **83**, 281 (1951); **87**, 795 (1952).
4. H. S. W. Massey, *Electronic and Ionic Impact Phenomena* (Clarendon, Oxford, 1969), vol. II.
5. L. B. Loeb, *Basic Processes of Gaseous Electronics* (Univ. of California Press, Berkeley, CA, 1960).
6. E. W. McDaniel and E. A. Mason, *The Mobility and Diffusion of Ions in Gases* (Wiley, New York, 1973); see also E. A. Mason and E. W. McDaniel, *Transport Properties of Ions in Gases* (Wiley, New York, 1988).
7. H. H. Hill Jr., W. F. Siems, R. H. St. Louis, D. G. McMinn, *Anal. Chem.* **62**, 1201 (1990).
8. R. H. St. Louis and H. H. Hill, *Crit. Rev. Anal. Chem.* **21**, 321 (1990).
9. G. A. Eiceman, *ibid.* **22**, 17 (1991).
10. Z. Karpas, *Forensic Sci. Rev.* **1**, 103 (1990).
11. P. R. Kemper and M. T. Bowers, *J. Am. Soc. Mass Spectrom.* **1**, 197 (1990).
12. N. Aristov and P. B. Armentrout, *J. Am. Chem. Soc.* **109**, 1806 (1986).
13. P. R. Kemper and M. T. Bowers, in preparation.
14. T. G. Dietz, M. A. Duncan, D. E. Powers, R. E. Smalley, *J. Chem. Phys.* **74**, 6511 (1981); V. E. Bondybey and J. H. English, *ibid.* **76**, 2165 (1982).
15. P. P. Radi, G. von Helden, M.-T. Hsu, P. R. Kemper, M. T. Bowers, *Int. J. Mass Spectrom. Ion Processes* **109**, 49 (1991).
16. The quantity σ is really the collision cross section only for "hard sphere" collisions of large ions with He. For smaller species, such as transition metal ions, σ is really the collision integral, which requires consideration of the details of the interaction potential.
17. Equation 2 holds for heavy ions colliding with light neutrals for relatively low values of E. These conditions are fulfilled for all systems reported in this article.
18. P. R. Kemper and M. T. Bowers, *J. Phys. Chem.* **95**, 5134 (1991).
19. ———, *J. Am. Chem. Soc.* **112**, 3231 (1990).
20. Early papers that document the involvement of excited electronic states: W. D. Reents, Jr., F. Stroble, R. B. Freas, J. Wronka, D. P. Ridge, *J. Phys. Chem.* **89**, 5666 (1985); J. L. Elkind and P. B. Armentrout, *ibid.*, p. 5626.
21. For a recent review, see P. B. Armentrout, *Annu. Rev. Phys. Chem.* **41**, 313 (1990).
22. P. A. M. van Koppen, P. R. Kemper, M. T. Bowers, *J. Am. Chem. Soc.* **114**, 1083 (1992).
23. ———, *ibid.*, p. 10941.
24. P. R. Kemper, M.-T. Hsu, M. T. Bowers, *J. Phys. Chem.* **95**, 10600 (1991).
25. P. A. M. van Koppen, P. R. Kemper, M. T. Bowers, *J. Am. Chem. Soc.*, in press.
26. P. A. M. van Koppen, *et al.*, *ibid.* **112**, 5663 (1990); *ibid.* **115**, 2359 (1991).
27. S. K. Loh, E. R. Fisher, L. Lian, R. H. Schultz, P. B. Armentrout, *J. Phys. Chem.* **93**, 3159 (1989).
28. P. R. Kemper, J. Bushnell, G. von Helden, M. T. Bowers, *ibid.* **97**, 52 (1993).
29. G. von Helden, P. R. Kemper, M.-T. Hsu, M. T. Bowers, *J. Chem. Phys.* **96**, 6591 (1992).
30. H. Partridge, C. W. Bauschlicher, Jr., S. R. Langhoff, *J. Phys. Chem.* **96**, 5350 (1992).
31. W. Weltner and R. van Zee, *Chem. Rev.* **89**, 1713 (1989), and references therein.
32. D. C. Parent and S. L. Anderson, *ibid.* **92**, 1541 (1992), and references therein.
33. For a recent summary, see M. F. Jarrold, *Science* **252**, 1085 (1991).
34. For detail on the structural model and in-depth discussion on mobility versus cluster size, see G. von Helden, M.-T. Hsu, N. G. Gotts, M. T. Bowers, *J. Phys. Chem.*, in press; see also G. von Helden, M.-T. Hsu, P. R. Kemper, M. T. Bowers, *J. Chem. Phys.* **95**, 3835 (1991).
35. Actually, the sum of the van der Waals radii of C and He needed to be specified for the calculations. On the basis of published values, we chose 1.15 Å for He and 1.55 Å for C for a sum of 2.7 Å, which then was not varied.
36. H. W. Kroto, J. R. Heath, S. C. O'Brien, R. F. Curl, R. E. Smalley, *Nature* **318**, 162 (1985), Q. L. Zhang *et al. J. Phys. Chem.* **90**, 525 (1986).
37. R. E. Smalley, *Acc. Chem. Res.* **25**, 97 (1992).
38. G. von Helden, M.-T. Hsu, N. G. Gotts, P. R. Kemper, M. T. Bowers, *Chem. Phys. Lett.*, in press.
39. C. J. Brabec *et al.*, *Phys. Rev. B* **46**, 7326 (1992).
40. G. von Helden, N. G. Gotts, M. T. Bowers, *Nature* **363**, 60 (1993); *J. Am. Chem. Soc.*, in press.
41. The first annealing studies in which IC was used were reported by M. F. Jarrold and H. C. Honea [*J. Am. Chem. Soc.* **114**, 459 (1992)].

42. M. Feyereisen, M. Gutowski, J. Simons, J. Almlöf, *J. Chem. Phys.* **96**, 2926 (1992); see also X. Jing and J. R. Chelikowski, *Phys. Rev. B* **46**, 15503 (1992).
43. Supported by National Science Foundation grant CHE92-19752 and Air Force Office of Scientific Research grant AFOSR92-J-0021.

True Atomic Resolution by Atomic Force Microscopy Through Repulsive and Attractive Forces

F. Ohnesorge and G. Binnig

The (10$\bar{1}$4) cleavage plane of calcite has been investigated by atomic force microscopy in water at room temperature. True lateral atomic-scale resolution was achieved; the atomic-scale periodicities as well as the expected relative positions of the atoms within each unit cell were obtained. Along monoatomic step lines, atomic-scale kinks, representing point-like defects, were resolved. Attractive forces on the order of 10^{-11} newton acting between single atomic sites on the sample and the front atoms of the tip were directly measured and provided the highest, most reliable resolution on a flat, well-ordered surface.

Atomic force microscopy (AFM) (*1*, *2*) is capable of resolving surface structures of both conductors and insulators on the atomic scale in air, in ultrahigh vacuum (UHV), and in liquids [for an overview see (*3*–*5*)]. The development of AFM in liquids by the group of Hansma (*6*) has largely extended the range of applications for this technique especially in the fields of biology (*7*–*9*) and electrochemistry (*10*). Imaging surfaces by AFM has proven to be a powerful tool in a number of fields [for an overview, see: (*3*–*5*, *11*, *12*)] because many materials under certain conditions are not accessible by any other technique in the size range from <1 to 50 nm. Many atomic-scale images of crystalline solids taken by AFM have been published. However, most of the reported data show either perfectly ordered periodic atomic structures or defects on a larger lateral scale, but no well-defined, laterally resolved atomic-scale defects like those seen in images routinely obtained with scanning tunneling microscopy (STM). Although STM and AFM are very much alike in many respects, there are significant differences between the two methods, and the question has been raised whether the AFM is really a microscope like the STM with true atomic resolution (*3*).

In this article we describe investigations on calcite ($CaCO_3$) in water at room temperature. Calcite has already been studied by AFM in liquids. The main emphasis has been on crystal growth and dissolution processes on the atomic scale (*13*), but some studies have focused on atomic-surface structure analysis (*14*). In the results presented here, well-defined defects were observed with true atomic-scale lateral resolution. This resolution could only be achieved when the estimated net repulsive loading force exerted on the sample by the front atoms of the tip was 10^{-10} N or lower. Upon increasing the force, we observed that monoatomic steplines were slowly wiped away and a perfectly ordered surface was left (*15*). This observation explains why mostly defect-free atomic resolution has been observed with AFM. In most of the reported results, repulsive forces greater than 10^{-10} N have been applied by the front atoms of the tip.

Experimental Results

We used a home-built AFM with optical lever detection as described briefly in (*16*) together with commercially available (*17*) force sensors with integrated tips. Calcite cleaves easily to form a macroscopic (10$\bar{1}$4) cleavage rhombohedron. The structure of the (10$\bar{1}$4) cleavage plane, which does not cross any of the strong covalent C–O bonds, is shown in Fig. 1 as derived from the three-dimensional crystal data (*18*).

The authors are in the IBM Research Division, Physikgruppe München, Schellingstrasse 4, 8000 München 40, Federal Republic of Germany.

The small amount of Millipore water used (<20 μl) covered a fairly large (~0.5 cm^2) freshly cleaved calcite surface and should have equilibrated with the $CaCO_3$ rather quickly at room temperature. Relatively stable imaging was possible within a few minutes after adding the liquid. If we assume that the oxygen atoms raised above the (10$\bar{1}$4) plane (shown in black in Fig. 1) strongly dominate the contrast seen by the AFM, one should expect to find a rectangular surface symmetry with parameters |**a**| = 8.1 Å and |**b**| = 5.0 Å and two oxygen atoms per unit cell.

Detecting single oxygen sites on such a structure will require very gentle forces between the front atom of the tip and the sample to avoid elastic or even destructive deformations. However, under typical imaging conditions the tip senses rather strong attractive forces, such as van der Waals or capillary forces. Therefore, in most cases the measured cantilever deflection plotted versus the relative sample position exhibits a typical hysteresis between approach and retract trace (*19, 20*): When the tip is brought very close to the sample, the second derivative (absolute value) of the attractive force interaction potential exceeds the force constant of the cantilever spring and the tip jumps toward the sample surface. Usually these longer range attractive background forces pull the tip so strongly toward the sample that its topmost atoms become pressed against the sample with forces greater than they might withstand. By slightly retracting the sample, that is, by applying a negative overall loading force to the cantilever, the forces can be partially balanced to reduce the effective net repulsive force on the topmost atoms. When the sample is retracted well beyond the "jump into contact" point, the cantilever will jump back. Because of this instability during the tip sample approach, there is an inaccessible tip sample separation regime at small distances of roughly several tens of angstoms. This instability can be avoided by using sufficiently stiff cantilevers which, of course, would lower the resolution of the instrument. The inaccessible regime can also be reduced by minimizing the attractive background forces acting on the tip. Operating the AFM in liquids (*20*) or in UHV eliminates the capillary forces caused by water or similar films on surfaces. Choosing appropriate media between the tip and the sample makes it possible to vary the Hamaker constants in order to minimize the attractive van der Waals forces; the resulting forces can even become repulsive (*21–24*). We note that active force compensation techniques have also been investigated for balancing long-range tip sample interactions (*25*).

During the measurements reported here, the longer range attractive interaction between the tip and the sample was so small that even for a relatively soft cantilever spring (force constant 0.2 N/m) no such instability was measured (force resolution of the instrument was 0.1 × 10^{-11} to 0.2 × 10^{-11} N for DC to 10 kHz operating conditions). Images could be recorded at any desired separation d between the tip's front atom and the sample. Upon approaching the sample, when thermal drifts had reached a minimum of ~0.1 Å/s after ~1 hour of operation, the cantilever proceeded continuously without instability from far away, where no tip sample interaction could be measured, to a separation regime where overall attractive forces were detected. Finally, the overall repulsive regime was reached. This behavior is shown in Fig. 2, which plots the overall force F as measured by the cantilever deflection S versus the vertical relative sample position z. Overall attractive forces were measured beginning at a sample position of about $z \leq 12$ Å before that point—chosen to be $z = 0$—where the transition to the overall repulsive regime occurred. At $z \approx 10$ Å, the attractive force gradient increased significantly. At $z \approx 3$ to 4 Å, the minimum of the $S(z)$ curve was reached. Approach and retract traces of the $S(z)$ curve coincided extremely well; therefore, only a single cycle is shown in Fig. 2. The cycle rate was ~0.1 Hz while the tip was scanning ~10 nm across the surface at ~40 Hz in the fast scan direction; therefore this $S(z)$ curve averages over many sample sites. The AFM working point on that $S(z)$ curve, that is, the set value for the mean force exerted on the sample by the tip, was selected with an approximate accuracy of below 1 × 10^{-11} N. The maximum attractive force at $z \approx 3$ to 4 Å of about −4.5 × 10^{-11} N is of the same order of magnitude as the expected van der Waals attraction between two single atoms at equilibrium separation (*21*). Thus only one or at most a few tip atoms can have contributed to this $S(z)$ curve, at least at $z > 4$ Å.

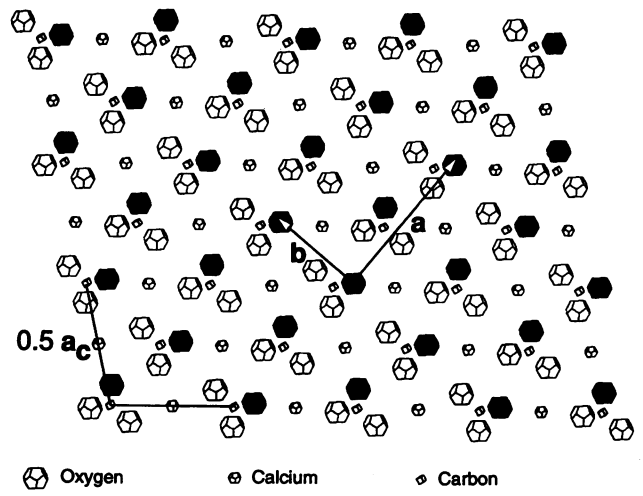

Fig. 1. A model of the (10$\bar{1}$4) cleavage plane of calcite derived from three-dimensional crystal data (*18*). The carbon atoms as centers of the carbonate ions and the calcium ions span this plane with an oblique lattice symmetry with parameters of $|\mathbf{a}_c| = 2 \times 6.41$ Å and $\gamma = 101.9°$. Both different spatial orientations of the carbonate ions result in one oxygen lying in this (10$\bar{1}$4) plane, one below and one above this crystal plane by ~1 Å. Assuming only the latter, marked in black in the figure, were visible for the AFM tip, a rectangular symmetry with |**a**| = 8.1 Å and |**b**| = 5.0 Å with two oxygen atoms per unit cell has to be expected in the AFM image.

The inset in Fig. 2 shows three $S(z)$ curves measured at a cycle rate of ~540 Hz while the tip was scanning very slowly across the sample at a velocity of ~1 Å/s. The displayed oscilloscope $S(z)$ traces were averaged over about four cycles. Three characteristic kinds of approach-retract cycles could be distinguished: $S(z)$ curves like type I and III were recorded only at laterally sharply confined atomic sites on the sample, whereas anywhere else on the sample an intermediate force-versus-distance behavior like that in curve II was observed. This observation is consistent with the "sample site–averaged" $S(z)$ measurement described above. The type I $S(z)$ curves were observed to repeat with spatial periodicity (see below). The curves I to III represent measurements of the force interaction between tip and sample at atomic-scale lateral resolution.

This observed behavior of the tip sample interaction is remarkable in that the attractive forces are usually stronger by at least one order of magnitude and start to be detected much further away from the sample. We believe that using very sharp tips (nominal tip radius ≈ 100 Å) made the extremely small long-range attractive background forces possible. Additionally, van der Waals attraction is screened in a medium such as water by roughly one order of magnitude (*21*). Effects due to electric double-layer repulsion may also play a role. Furthermore, immediately immersing the freshly cleaved crystals in purified water established relatively well defined conditions. It has to be remarked that for deriving the actual interaction curve $F(d)$, one has to take account of elastic deformation

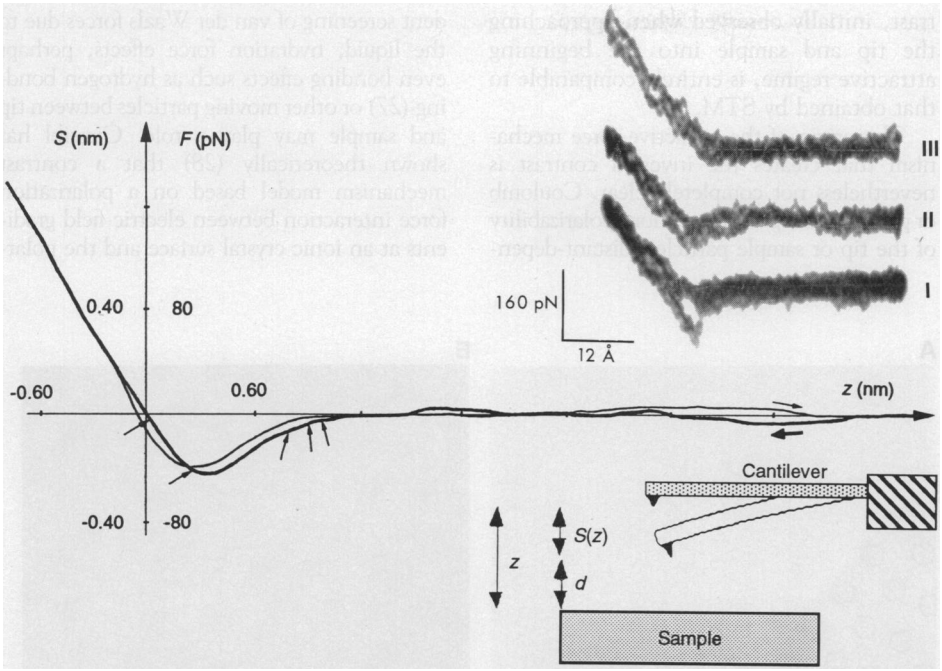

Fig. 2. The interaction between tip and sample is described by plotting the overall force F sensed by the tip as measured by the cantilever deflection S versus the vertical relative sample position z. The cantilever's force constant is k = 0.2 N/m (*17*). The zero force point is measured for large tip-sample separations; negative values correspond to attractive overall forces and positive values correspond to repulsive overall forces acting on the tip. The z = 0 point was chosen as that sample position at which the transition from attractive to repulsive deflection of the lever occurred. Approach (thick line) and retract trace (thin line) do not show any instability or significant hysteretic behavior. The $S(z)$ cycles were measured at a cycle rate of ~0.1 Hz while the tip was scanning at a velocity of ~200 nm/s. Only a single cycle is shown. The AFM working points on the $S(z)$ curve indicated by arrows are, from left to right, the points at which Figs. 3H, 5A, 3E, 3C, and 3B were taken. The tolerance of the z calibration of the piezo was ~10%. Inset: Force-versus-distance curves at different atomic-scale lateral-sample positions. The approach-retract cycle rate was 540 Hz while the tip was scanning very slowly at about 1 Å per second. Traces like curves 1 and 3 were recorded only laterally at extremely sharply confined sites on the sample. Anywhere else on the sample a trace like that in curve 2 was observed, consistent with the main curve shown.

of tip and sample material even at these small forces. Single interatomic force constants are roughly of the order of 10 N/m. At an atomic site, the spring constant will in effect be even much smaller because the local environment of the site will be deformed as well.

The images shown in Fig. 3 were taken at different working points along the $S(z)$ curve, as indicated correspondingly in Fig. 2. Here, as is usual for AFM images, dark spots in the gray-scale data representation correspond to sample locations where the tip has been pulled toward the sample and vice versa. The AFM was operated in the so-called variable-deflection mode, where the immediate lever deflection is recorded as the signal data and no feedback control is applied to the z position of sample. If an atomic site locally attracts the lever toward the sample (that is, the site appears as a dark spot), we define the contrast as inverted. In order to obtain Fig. 3A, the tip was slowly moved toward the sample into a region where contrast first started to be observed at all, approximately at $z \approx 10$ Å. Exclusively attractive forces generated the (inverted) contrast; dark spikes representing laterally extremely localized attractive forces were detected, in between which no contrast was measurable. The positions of the spikes already represent quite well the lattice formed by the oxygen atoms above the (10$\bar{1}$4) cleavage plane, because one has to take into account that the diameter of an oxygen atom (~1 Å) far exceeds the lateral extent of these spikes. We assume that these are the type I $S(z)$ curve sites (Fig. 2) because of the agreement in peak depth and in lateral extent and distribution. Upon further approach, the deep spikes (reminiscent of delta functions) begin to convert to dark peaks with larger diameter, now excellently representing the expected oxygen lattice (Fig. 3, B and C). The depth of these peaks appears to be cut off, probably because the front of the tip would now begin to touch the sample surface. The measured peak depth of about 2.0 to 3.0 Å roughly corresponds to moving from the working point into the vicinity of the minimum on the $S(z)$ curve, if one assumes $\Delta d \approx \Delta z$ by neglecting elastic deformations of tip and sample. This result provides a first indication for the tip's front atom possibly starting to sense net repulsive forces already close to the minimum of the $S(z)$ curve. In Fig. 3, A and B, the gray level between the dark spots corresponds to practically zero attractive force ($<1 \times 10^{-11}$ N), meaning that the contrast originates solely from single atomic sites on the sample locally exerting net attractive forces of about 4.0×10^{-11} to 6.0×10^{-11} N on the front atoms of the tip.

When further reducing z, spots brighter than the initial gray level become visible next to the dark peaks (Fig. 3, D and E). Apparently the upstanding oxygen atoms now start to contribute noninverted contrast by contact interaction of the tip's front atom with the sample. In Fig. 3F, dark spikes are visible again, apparently superimposing a second image of the oxygen lattice, which is slightly displaced compared to the primary image. We believe this can be understood as a secondary microtip starting to image the oxygen lattice just like the primary tip in Fig. 3A. However, these attractive forces now have to overcome a compression of the primary tip against the sample. Continuously approaching the sample further (Fig. 3, G and H), various kinds of images with unreliably changing structures within the unit cell are observed, now predominantly at noninverted contrast. Apparently the secondary tip and perhaps a few more microtips, which are probably all single imaging atoms, have started to increasingly contribute to the noninverted contrast. This most likely indicates that now the front atom of the tip senses net repulsive forces, since then the elastic deformation of tip and sample would increase the probability for multitip contributions by compressing tip and sample material. Results obtained by AFM usually show the correct lattice periodicities but, at high repulsive loads, here for $z << 3$ to 4, Å, unreliably altered relative positions of the atoms within the unit cell are apparently measured because of multitip effects (*26*). In contrast, we obtained the same structure representing the correct oxygen positions with different tips and varying tip conditions as often as desired in the attractive mode with inverted contrast at sample positions 10 Å $> z >$ 4 Å corresponding to a small attractive tip-sample interaction ranging from -4.5×10^{-11} to -1.0×10^{-11} N. Elastic deformation of tip and sample material due to net attractive forces acting between the tip's front atom and the sample atoms, thus pulling them toward each other, would further lower the tendency for multitip contributions and therefore improve the effective tip properties.

Mechanistic Considerations

In Fig. 4, the data shown in Fig. 3D have been replotted with the gray-scale represen-

tation inverted, that is, bright spots correspond to sample locations where the tip has been attracted toward the sample and vice versa. The excellent agreement of the data with the known crystal model of the (10$\bar{1}$4) cleavage plane of calcite is emphasized by including the schematic rescaled from Fig. 1 into a unit cell averaged section of the data. The lattice formed by the upstanding oxygen atoms of each carbonate as well as the positions of the calcium ions are visible. This observation of the true unit cell structure provides profound evidence of true atomic-scale lateral resolution: There is practically zero probability for a multitip artificially first to generate the oxygen unit cell and, upon further tip sample approach, for the imaged unit cell to contain the two additional calcium sites. Therefore, we have detected attractive force interactions with the imaging tip that are laterally confined to single atom sites on the sample, particularly by taking into account the maximum measured attractive force (Fig. 2). This attractive force is of the order of the value expected for the van der Waals attraction of two atoms at equilibrium separation and, in the case of purely inverted contrast, nonzero cantilever deflection is sensed only at the atomic sites (Fig. 3, A and B). The quality of the inverted contrast, initially observed when approaching the tip and sample into the beginning attractive regime, is entirely comparable to that obtained by STM.

The origin of the attractive force mechanism that creates the inverted contrast is nevertheless not completely clear. Coulomb or permanent dipole interaction, polarizability of the tip or sample particles, distant-dependent screening of van der Waals forces due to the liquid, hydration force effects, perhaps even bonding effects such as hydrogen bonding (*27*) or other moving particles between tip and sample may play a role. Giessibl has shown theoretically (*28*) that a contrast mechanism model based on a polarization force interaction between electric field gradients at an ionic crystal surface and the polar-

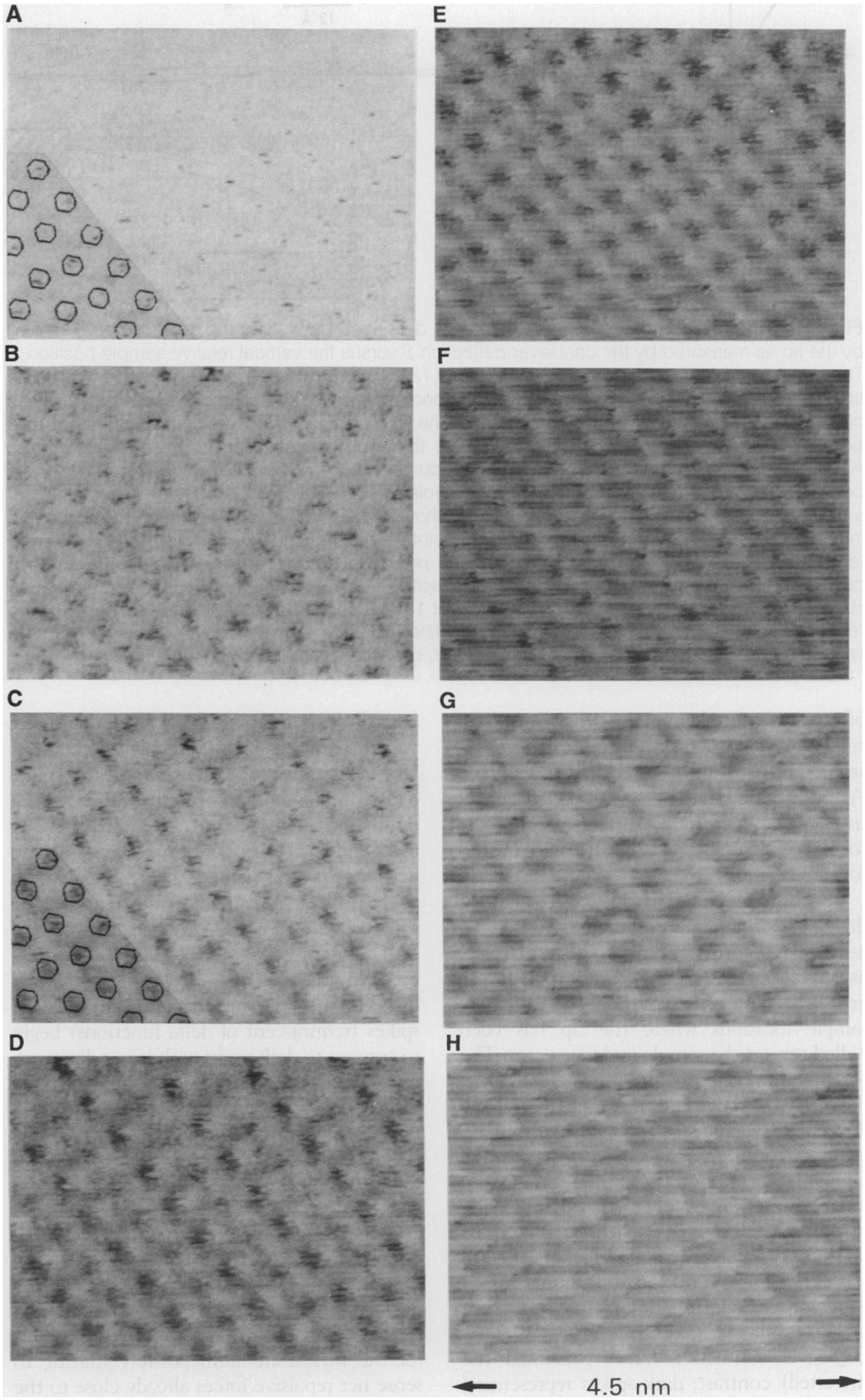

Fig. 3. (**A** to **H**) All data were taken in the variable deflection mode in purified water at room temperature and only raw data are shown. Scan size is 4.5 nm by 3.4 nm. While recording this image sequence, the sample was continuously approached toward the tip starting far away at zero force. The very slow approach was continued also during scanning the individual images from top to bottom (scan rate was about 4 seconds per frame). (A) Upon approaching the sample (that is, lowering *z*), image contrast is first detected at $z \approx 10$ Å exclusively in the form of dark spikes corresponding to a locally sharply enhanced attractive force acting on the tip. These spikes already represent the lattice formed by the upstanding oxygen atoms; a model rescaled from Fig. 1 is included showing only those oxygens with a diameter of ~1 Å. (B and C) After further tip sample approach, the deep delta function–like spikes start to convert to dark contrast peaks with larger diameter, showing the expected oxygen lattice. The zigzag along lattice vector **a** should be noted. (D and E) Noninverted contrast starts to contribute, but the inverted contrast still dominates. (F) Additional dark spikes become visible at the oxygen sites, probably due to a secondary tip starting to contribute in the same way as the primary tip in (A). It has to be remarked that while increasing the force settings, the average gray level had to be readjusted from (F) to (G) in order to keep the contrast within the dynamic range of the data acquisition system. Most likely because of multitip contributions, (G) and (H) show distorted structures within the unit cell, now predominantly at noninverted contrast.

izability of the tip should in principle provide atomic resolution in the attractive regime. If we assume further that a polarization force interaction also involving a polarizability of the sample ions is—at least partially—responsible for the imaging contrast, the slightly alternating appearance of the rows parallel to lattice vector **b** in the attractive imaging mode, visible in Fig. 4, can be understood. Almost any anisotropic polarizability or permanent dipole moment of the tip interacting with the alternating permanent dipole moments and polarizability tensors related to the alternating carbonate sites when going along lattice vector **a** will lead to an alternating contrast appearance.

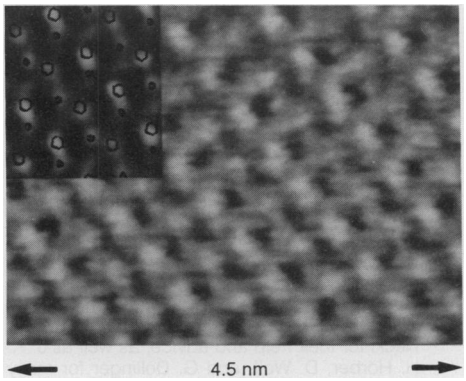

Fig. 4. These data are the same as in Fig. 3D. However, for better visualization, the gray-scale representation of the data has been inverted. Bright spots in this figure correspond to sample locations where the tip has been strongly pulled toward the surface from its average deflection. Slight low-pass filtering has been applied. Excellent agreement of the data with the expected surface structure is found. A unit cell averaged section of the data has been added with the surface lattice model included. The model was reduced to show only the upstanding oxygens and the calcium ions. The parameters of the lattice formed by the upstanding oxygens were measured to be $|\mathbf{a}|$ = 7.9 to 8.5 Å and $|\mathbf{b}|$ = 4.9 to 5.2 Å. The scan size is 4.5 nm by 3.4 nm.

Imaging Defects

A very clear-cut proof for true atomic-scale lateral resolution is the observation of a well-defined defect. Such data are presented in Fig. 5. A monoatomic as well as a diatomic step is visible in one image. Images like Fig. 5A were taken in the so-called constant force mode, commonly used in AFM. A feedback circuitry appropriately responding to noninverted contrast (upstanding features on the surface deflect the tip upward) controlled the sample position z in order to maintain the lever deflection S constant. Therefore, the sample had to be approached into a z position (indicated in Fig. 2), where the tip senses the appropriate force gradient. At the monoatomic kinked step with a measured height of about 2.7 to 3.3 Å (theoretical value 3.16 Å), single unit cells are clearly resolved (Fig. 5B). The measured phase shifts (that is, the parallel displacement) between lattice vectors of adjacent crystal planes when crossing the step line match the expected values well. The phase shift between crystal rows parallel to lattice vector **a** when crossing the step at a kink along **a** is measured to be 2.1 to 2.9 Å. Crossing the step along **b** the phase shift between the rows parallel to **b** is 2.8 to 3.7 Å; the alternating appearance of the crystal rows parallel to **b** should be noted. The values from 3D crystal data are 2.5 and 3.5 Å, respectively. Abruptly terminating rows forming kinks along the step line even represent point defects.

At diatomic steps (such as in Fig. 5) with a total measured height of 5.2 to 6.5 Å, the phase shifts cannot be determined as accurately as for monosteps. Bigger steps appear more disturbed because rougher surfaces are less well resolved by STM or AFM due to the tip geometry. The appearance of the structure within the unit cell is slightly distorted. According to the discussion above, this distortion occurs because the loading forces could not be kept at the lowest level when imaging in the constant force mode. Therefore the front atom of the tip has probably already experienced a small net repulsive force ($<<10^{-10}$ N), and hence does not provide the highest achievable resolution, although step structures could be reproducibly imaged. Inverted feedback response could be used in future studies so that the smallest but extremely sensitive attractive interactions between the front atom of the tip and the sample could also be used for extremely gentle attractive force imaging in the constant force mode. From the fact that the monostep is clearly resolved, even showing kinks that can be viewed as point defects, we claim to have achieved a true lateral resolution of better than the size of a unit cell also in the constant force mode, which means 8.1 Å along **a** and 5.0 Å along **b**.

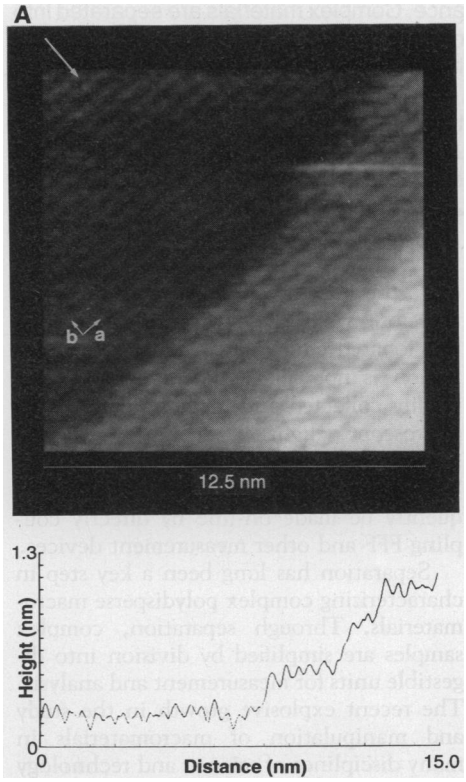

Fig. 5. (**A**) For well-calibrated height measurements, this image is taken in the constant force mode at $z \approx 2.5$ Å (Fig. 2). Noninverted contrast is measured. Bright structures in the gray-scale representation of this figure correspond to a lever deflection away from the sample. Image field is 12.5 nm by 12.5 nm. The height of the step along the diagonal of the frame is measured to be about 2.7 to 3.3 Å, the second stepline in the lower right corner is found to be 5.2 to 6.5 Å high. (**B**) A trace along the cross section as indicated by the arrow in the upper left corner of the image is shown. The height of a monostep as expected from the three-dimensional crystal data is 3.16 Å. The apparent atomic corrugation is measured to be approximately 0.9 to 1.3 Å. When crossing a monoatomic stepline, the crystal model suggests the following phase shifts. On the upper terrace, the rows parallel to the lattice vector **a**, which are nominally separated from each other by 5.0 Å, should lie exactly in the middle between corresponding rows of the atomic layer below. This is found in the data of (A) (accuracy approximately ±0.4 Å), clearly visible at the kinks. The phase shift between corresponding rows parallel to lattice vector **b**, which repeat with 8.1 Å, theoretically ought to be 3.5 Å when crossing a monostep. The measured values range roughly from 2.8 to 3.7 Å; the alternating appearance of these rows should be noted.

Summary

Extremely small long-range background forces were measured between the imaging tip of the AFM and the sample surface in an aqueous environment. No instability occurred when approaching the sample toward the tip. Atomic force images could be recorded at any desired tip sample separation. Attractive forces on the order of 10^{-11} N acting between single atomic sites on the sample surface and the front atom of a tip were measured directly. Under these well-controlled conditions, a kinked monoatomic stepline was observed with true atomic-scale lateral resolution. Atomic resolution that showed STM-like reliability was achieved, particularly in the attractive-force regime.

REFERENCES AND NOTES

1. G. Binnig, C. F. Quate, C. Gerber, *Phys. Rev. Lett.* **56**, 930 (1986).
2. G. Binnig, C. Gerber, E. Stoll, T. R. Albrecht, C. F. Quate, *Europhys. Lett.* **3**, 1281 (1987).
3. G. Binnig, *Ultramicroscopy* **42–44**, 7 (1992).
4. J. Frommer, *Angew. Chem. Int. Ed. Engl.* **31**, 1298 (1992).
5. D. Rugar and P. K. Hansma, *Phys. Today* **43** (no. 10), 23 (1990).
6. O. Marti, B. Drake, P. K. Hansma, *Appl. Phys. Lett.* **51**, 484 (1987).
7. B. Drake *et al.*, *Science* **243**, 1586 (1989).
8. W. Häberle, J. K. H. Hörber, G. Binnig, *J. Vac. Sci. Technol.* **B9**, 1210 (1991).
9. W. Häberle, J. K. H. Hörber, F. Ohnesorge, D. P. E. Smith, G. Binnig, *Ultramicroscopy* **42–44**, 1161 (1992).
10. S. Manne, P. K. Hansma, J. Massie, V. B. Elings, A. A. Gewirth, *Science* **251**, 183 (1991).
11. M. Radmacher, R. W. Tillmann, M. Fritz, H. E. Gaub, *Science* **257**, 1900 (1992).
12. D. Sarid, *Scanning Force Microscopy* (Oxford Univ. Press, New York, 1991).
13. G. Friedbacher, P. K. Hansma, E. Ramli, G. D. Stucky, *Science* **253**, 1261 (1991); P. E. Hillner, S. Manne, A. J. Gratz, P. K. Hansma, *Ultramicroscopy* **42–44**, 1387 (1992); P. E. Hillner, A. J. Gratz, S. Manne, P. K. Hansma, *Geology* **20**, 359 (1992); A. J. Gratz, P. E. Hillner, P. K. Hansma, *Geochim. Cosmochim. Acta* **57**, 491 (1993); P. E. Hillner, S. Manne, A. J. Gratz, P. K. Hansma, *Faraday Discuss. Chem. Soc.*, in press.
14. A. L. Rachlin, G. S. Henderson, M. C. Goh, *Am. Mineral.* **77**, 904 (1992).
15. F. Ohnesorge and G. Binnig, unpublished results.
16. F. Ohnesorge *et al.*, *Ultramicroscopy* **42–44**, 1236 (1992).
17. We used cantilevers made of crystalline silicon ("Ultralevers") from Park Scientific Instruments, Sunnyvale, CA 94089, which were 95 μm in length and 0.6 μm in thickness. The measured resonance frequencies of the cantilevers we used were within 2 to 3% of the nominal value of 77 kHz. The approximate tolerance of their normal spring constants is thus ~10%. See also J. P. Cleveland, S. Manne, D. Bocek, P. K. Hansma, *Rev. Sci. Instrum.* **64** (2), 403 (1993).
18. R. W. G. Wyckoff, *Crystal Structures* (Wiley, New York, 1964).
19. G. M. McClelland, R. Erlandsson, S. Chiang, in *Review of Progress in Quantitative Non-Destructive Evaluation*, D. O. Thompson and D. E. Chimenti, Eds. (Plenum, New York, 1987), vol. 6b, pp. 1307–1314
20. A. L. Weisenhorn, P. K. Hansma, T. R. Albrecht, C. F. Quate, *Appl. Phys. Lett.* **54**, 2651 (1989).
21. J. Israelachvili, *Intermolecular and Surface Forces* (Academic Press, London, ed. 2, 1991).
22. U. Hartmann, *Phys. Rev. B* **43**, 2404 (1991).
23. J. E. Dzyaloshinskii, E. M. Lifshitz, L. B. Pitaevskii, *Adv. Phys.* **10**, 165 (1961).
24. A. L. Weisenhorn, P. Maivald, H.-J. Butt, P. K. Hansma, *Phys. Rev. B* **45** (19), 11226 (1992).
25. S. A. Joyce and J. E. Houston, *Rev. Sci. Instrum.* **62**, 710 (1991).
26. F. F. Abraham, I. P. Batra, S. Ciraci, *Phys. Rev. Lett.* **60**, 1314 (1988); S. A. C. Gould, K. Burke, P. K. Hansma, *Phys. Rev. B* **40**, 5363 (1989); P. Rasch, W. M. Heckl, H. W. Deckman, W. Häberle, *Mater. Res. Soc. Symp. Proc.* **233**, 287 (1991).
27. J. H. Hoh, J. P. Cleveland, C. B. Prater, J.-P. Revel, P. K. Hansma, *J. Am. Chem. Soc.* **114**, 4917 (1991).
28. F. J. Giessibl, *Phys. Rev. B*, **45**, 13815 (1992).

29. We thank D. P. E. Smith, W. Häberle, and W. M. Heckl for their help and advice, as well as J. K. H. Hörber, D. Wolf, and G. Dollinger for many inspiring discussions.

Field-Flow Fractionation: Analysis of Macromolecular, Colloidal, and Particulate Materials

J. Calvin Giddings

Field-flow fractionation (FFF) is a family of flexible elution techniques capable of simultaneous separation and measurement. Its sample domain extends across a broad macromolecular-colloidal-particulate continuum from about 1 nanometer to more than 100 micrometers and incorporates both simple and complex macromaterials of biological, biomedical, industrial, and environmental relevance. Complex materials are separated into components to simplify measurement. Component properties measurable by FFF include mass, size, density, charge, diffusivity, and thickness of adsorbed layers. When characterization by these properties is inadequate, other measurement tools can be readily coupled to FFF, either off-line or on-line, by virtue of its flow-elution operation. This article describes the principles and major subtechniques of the FFF family along with application of its measurement and separative capabilities.

Field-flow fractionation is a relatively new family of techniques designed to disentangle and probe the physical and compositional structure of complex macromolecular, colloidal, and particulate materials (*1–10*). These tasks are approached through broad capabilities for both separation and measurement. Species can be separated in the 10^5-fold size range from $\sim 10^{-3}$ to 10^2 μm. The separation occurs by differential retention in a stream of liquid flowing through a thin channel. The separated components are eluted one at a time into a detector. The observed retention time t_r is related (often rigorously) to various physicochemical properties of the retained species; the measurement of t_r values can therefore yield these properties for each fractionated component. If this characterization is not sufficient, fractions can be readily collected and further examined by microscopy, light scattering, elemental analysis, subsequent FFF steps, and so on. The additional characterization can frequently be made on-line by directly coupling FFF and other measurement devices.

Separation has long been a key step in characterizing complex polydisperse macromaterials. Through separation, complex samples are simplified by division into digestible units for measurement and analysis. The recent explosive growth in the study and manipulation of macromaterials in many disciplines of science and technology demands improved separation tools with greater range, resolution, and versatility. The FFF process fulfills many of these needs by providing high selectivity and speed, simultaneous measurement, simplified coupling to other measurement devices, automation, ready fraction collection, applicability to diverse samples over a broad mass-size range, gentleness in separating delicate species, and flexibility in targeting specific problem areas. In addition, FFF is intrinsically simple and theoretically tractable. As a result, theory provides many useful guidelines for experiment and it underlies a broad capability for measurement (see below).

The FFF process was first conceptualized in the 1960s (*11*); accounts of the invention and subsequent work have been published (*6, 12, 13*). A couple of decades were required to gain a working base of FFF subtechniques (*13*) and to adapt instrumentation and procedures to experimental needs. Three recent international symposia on FFF (*14*) have highlighted the many important applications that are rapidly emerging (see below).

Although FFF is still at an early stage of development, the ensemble of techniques and applications are already remarkably diverse. Inherent diversity is a long-term strength of FFF. Unfortunately, diversity has so diluted focus that FFF is not now utilized for many promising applications because experimental precedence and protocols are lacking. Examples given below are suggestive of new possibilities.

Mechanism of FFF

The FFF mechanism combines elements of chromatography and field-driven techniques such as electrophoresis and ultracentrifugation (*1–10, 15*). Like chromatography, FFF is an elution technique with un-

The author is with the Field-Flow Fractionation Research Center, Department of Chemistry, University of Utah, Salt Lake City, UT 84112.